



1 **Improving thermodynamic profile retrievals from microwave**
2 **radiometers by including Radio Acoustic Sounding System (RASS)**
3 **observations**

4
5
6
7
8
9
10
11
12
13
14
15
16
17
18
19
20
21
22

Irina V. Djalalova^{1,2}, David D. Turner³, Laura Bianco^{1,2},
James M. Wilczak², James Duncan^{1,2}, Bianca Adler^{1,2} and Daniel Gottas²

¹Cooperative Institute for Research in Environmental Sciences (CIRES), Boulder, CO, USA

²National Oceanic and Atmospheric Administration, Physical Sciences Laboratory, Boulder, CO, USA

³National Oceanic and Atmospheric Administration, Global Systems Laboratory, Boulder, CO USA

Corresponding author address: Irina V. Djalalova (Irina.V.Djalalova@noaa.gov), NOAA/Physical
Science Laboratory, 325 Broadway, mail stop: PSD3, Boulder, CO 80305. Tel.: 303-497-6238.
Fax: 303-497-6181.



23	Outline
24	Abstract
25	1. Introduction
26	2. XPIA dataset
27	2.1 MWR measurements
28	2.2 Radiosonde measurements
29	2.3 WPR-RASS measurements
30	2.4 BAO data
31	3. Physical retrievals
32	3.1 Iterative retrieval technique
33	3.2 PR's bias correction
34	3.3 Averaging kernel
35	4. Results
36	4.1 PRs statistical analysis
37	4.2 Statistical analysis of PRs compared to NN retrievals
38	4.3 Statistics for the least close to the climatological profiles
39	4.4 Virtual temperature statistics
40	5. Conclusions
41	Data availability
42	Author contribution
43	Acknowledgments
44	References



45 **Abstract**

46 Thermodynamic profiles are often retrieved from the multi-wavelength brightness
47 temperature observations made by microwave radiometers (MWRs) using regression methods
48 (linear, quadratic approaches), artificial intelligence (neural networks), or physical-iterative
49 methods. Regression and neural network methods are tuned to mean conditions derived from
50 a climatological dataset of thermodynamic profiles collected nearby. In contrast, physical-
51 iterative retrievals use a radiative transfer model starting from a climatologically reasonable
52 value of temperature and water vapor, with the model run iteratively until the derived
53 brightness temperatures match those observed by the MWR within a specified uncertainty.

54 In this study, a physical-iterative approach is used to retrieve temperature and humidity
55 profiles from data collected during XPIA (eXperimental Planetary boundary layer Instrument
56 Assessment), a field campaign held from March to May 2015 at NOAA's Boulder Atmospheric
57 Observatory (BAO) facility. During the campaign, several passive and active remote sensing
58 instruments as well as in-situ platforms were deployed and evaluated to determine their
59 suitability for the verification and validation of meteorological processes. Among the deployed
60 remote sensing instruments was a multi-channel MWR, as well as two radio acoustic sounding
61 systems (RASS), associated with 915-MHz and 449-MHz wind profiling radars.

62 Having the possibility to combine the information provided by the MWR and RASS
63 systems, in this study the physical-iterative approach is tested with different observational
64 inputs: first using data from surface sensors and the MWR in different configurations, and then
65 including data from the RASS. These temperature retrievals are also compared to those derived
66 by a neural network method, assessing their relative accuracy against 58 co-located radiosonde



67 profiles. Results show that the combination of the MWR and RASS observations in the physical-
68 iterative approach allows for a more accurate characterization of low-level temperature
69 inversions, and that these retrieved temperature profiles match the radiosonde observations
70 better than all other approaches, including the neural network, in the atmospheric layer
71 between the surface and 5 km AGL. Specifically, in this layer of the atmosphere, both root
72 mean square errors and standard deviations of the difference between radiosonde and
73 retrievals that combine MWR and RASS are improved by ~ 0.5 °C compared to the other
74 methods. Pearson correlation coefficients are also improved.

75

76

77

78

79

80

81

82

83

84

85

86

87

88



89 **1. Introduction**

90 To monitor the state of the atmosphere for process understanding and for model
91 verification and validation, scientists rely on observations from a variety of instruments, each
92 one having its set of advantages and disadvantages. Using several diverse instruments allows
93 one to monitor different aspects of the atmosphere, while combining them in an optimized
94 synergetic approach can improve the accuracy of the information we have on the state of the
95 atmosphere.

96 During the eXperimental Planetary boundary layer Instrumentation Assessment (XPIA)
97 campaign, an U.S. Department of Energy sponsored experiment held at the Boulder
98 Atmospheric Observatory (BAO) in Spring 2015, several instruments were deployed (Lundquist
99 et al., 2017) with the goal of assessing their capability for measuring flow within the
100 atmospheric boundary layer. XPIA investigated novel measurement approaches, and quantified
101 uncertainties associated with these measurement methods. While the main interest of the XPIA
102 campaign was on wind and turbulence, measurements of other important atmospheric
103 variables were also collected, including temperature and humidity. Among the deployed
104 instruments were two identical microwave radiometers (MWRs) and two radio acoustic
105 sounding systems (RASS), as well as radiosondes launches that were used for verification.

106 MWRs are passive sensors, sensitive to atmospheric temperature and humidity content
107 that allow for a high temporal observation of the state of the atmosphere, with some
108 advantages and limitations. In order to estimate profiles of temperature and humidity, they
109 observe atmospheric brightness temperature and apply radiative transfer equations
110 (Rosenkranz, 1998) and neural network retrievals (Solheim et al., 1998a, and 1998b; Ware et al.,



111 2003), or physical retrieval methodologies that can include more information about the
112 atmospheric state in the retrieval process (Turner and Blumberg, 2019). Advantages of MWRs
113 include their compact design, the relatively high temporal resolution of the measurements (2-3
114 minutes), the possibility to observe the vertical structure of both temperature and moisture,
115 the deep layer of the atmosphere that can be monitored including during cloudy conditions,
116 and their capability to operate in a standalone mode. Disadvantages include the limited
117 accuracy, as the temperature and humidity profiles are not actively measured but retrieved,
118 their lower accuracy in the presence of rain because of scattering of radiation due to raindrops
119 in the atmosphere (and because some water can still deposit on the radome, although the
120 instruments use a hydrophobic radome and force airflow over the surface of the radome during
121 rain), rather coarse vertical resolution, and for retrievals the necessity to have a site specific
122 climatology. Other disadvantages include the challenges related to performing accurate
123 calibrations (Küchler et al., 2016, and references within), radio frequency interference (RFI), and
124 the low accuracy on the retrieved liquid water path (LWP) especially for values of LWP less than
125 50 g/m².

126 RASS, in comparison, are active instruments that emit a longitudinal acoustic wave
127 upward, causing a local compression and rarefaction of the ambient air. These density
128 variations are tracked by the Doppler radar associated with the RASS, and the speed of the
129 propagating sound wave is measured. The speed of sound is related to the virtual temperature
130 T_v (North et al., 1973), and therefore, RASS are routinely used to remotely measure vertical
131 profiles of virtual temperature in the boundary layer. Being an active instrument, the RASS is in
132 general more accurate than a passive instrument (Bianco et al., 2017), but they also come with



133 their sets of disadvantages. The main limitations of RASS for retrieval purposes are its low
134 temporal resolution (typically a 5-min averaged RASS profile is measured once or twice per
135 hour), and their limited altitude coverage. Recent studies (Adachi and Hashiguchi, 2019) have
136 shown that to make them more suitable to operate in urban areas RASS could use parametric
137 speakers to take advantage of their high directivity and very low side lobes. Nevertheless, the
138 maximum height reached by the RASS is still limited, being a function of both radar frequency
139 and atmospheric conditions (May and Wilczak, 1993), and is determined both by the
140 attenuation of the sound, which is a function of atmospheric temperature, humidity, and
141 frequency of the sound source, and the advection of the propagating sound wave out of the
142 radar's field-of-view. Therefore, data availability is usually limited to the lowest several km,
143 dependent on the frequency of the radar. In addition, wintertime coverage is usually
144 considerably lower than that in summer, due to a higher probability of stronger winds
145 advecting the sound wave away from the radar in the winter.

146 To get a better picture of the state of the temperature and moisture structure of the
147 atmosphere, it makes sense to try to combine the information obtained by both MWR and
148 RASS. Integration of different instruments has been of scientific interest for several years (Han
149 and Westwater 1995; Stankov et al. 1996; Bianco et al., 2005; Engelbart et al., 2009; Cimini et
150 al., 2020, Turner and Löhnert, 2020, to name some). In this study we particularly focus on the
151 combination of the MWR and RASS observations in the retrievals to improve the accuracy of
152 the temperature profiles in the lowest 5 km compared to the standard MWR retrievals
153 obtained through neural network (NN) processing, or compared to physical retrieval
154 approaches that do not include the information from RASS measurements.



155 This paper is organized as follows: Section 2 summarizes the experimental dataset;
156 Section 3 introduces the principles of the physical retrieval approaches used to obtain vertical
157 profiles of the desired variables; Section 4 produces statistical analysis of the comparison
158 between the different retrieval approaches and radiosonde measurement; finally, conclusions
159 are presented in Section 5.

160

161 2. XPIA data

162 The data used in our analysis were collected during the XPIA experiment, held in Spring
163 2015 (March-May) at the NOAA's Boulder Atmospheric Observatory (BAO) site, in Erie,
164 Colorado (Lat.: 40.0451 N, Lon.: 105.0057 W, El.: 1584 m MSL). XPIA was the last experiment
165 conducted at this facility, as after almost 40 years of operations the BAO 300-m tower was
166 demolished at the end of 2016 (Wolfe and Lataitis, 2018). XPIA was designed to assess the
167 capability of different remote sensing instruments for quantifying boundary layer structure, and
168 was a preliminary study as many of these same instruments were later deployed, among other
169 campaigns, for the second Wind Forecast Improvement Project WFIP2 (Shaw et al., 2019;
170 Wilczak et al., 2019) which investigated flows in complex terrain for wind energy applications,
171 and were for example used to study cold air pool and gap flow characteristics (Adler et al.,
172 2020; Banta et al., 2020; Neiman et al., 2019). The list of the deployed instruments included
173 active and passive remote-sensing devices, and in-situ instruments mounted on the BAO tower.
174 Data collected during XPIA are publicly available at <https://a2e.energy.gov/projects/xpia>. A
175 detailed description of the XPIA experiment can be found in Lundquist et al. (2017), while a



176 specific look at the accuracy of the instruments used in this study can be found in Bianco et al.
177 (2017).

178

179 **2.1 MWR measurements**

180 Two identical MWRs, managed by NOAA (MWR-NOAA) and by the University of
181 Colorado (MWR-CU), were deployed next to each other at the visitor center ~600 m south of
182 the BAO tower (see Lundquist et al., 2017 for a detailed map of the study area). Both MWRs
183 have 35-channels spanning a range of frequencies, with 21 channels in the lower (22-30 GHz) K-
184 band frequency band, and 14 channels in the higher (51-59 GHz) V-band frequency band.
185 Frequencies in the K-band are more sensitive to water vapor and cloud liquid water, while
186 frequencies in the V-band are sensitive to atmospheric temperature due to the absorption of
187 atmospheric oxygen (Cadeddu et al., 2013). Both MWRs observed at the zenith and at 15- and
188 165-degree elevation angles in the north-south plane (referred to as oblique elevation scans
189 hereafter; note zenith views have 90-degree elevation angles). In addition, each MWR was
190 provided with a separate surface sensor to measure pressure, temperature, and relative
191 humidity at the installation level that was ~2.5 m above ground level (AGL). MWRs are passive
192 devices which record the natural microwave emission in the water vapor and oxygen
193 absorption bands from the atmosphere, providing measurements of the brightness
194 temperatures. Vertical profiles of temperature (T), water vapor density (WVD), and relative
195 humidity (RH) were retrieved in real-time during XPIA every 2-3 minutes using a NN approach
196 provided by the private manufacturing company Radiometrics (Solheim et al. 1998). The NN
197 used a training dataset based on a 5-year climatology of profiles from radiosondes launched at



198 the Denver International Airport, 35 miles south-east from the XPIA site. NN-based MWR
199 vertical retrieval profiles were obtained using the zenith and an average of two oblique
200 elevation scans, all extending for 58 levels up to 10 km, with nominal vertical levels depending
201 on the height (every 50 m from the surface to 500 m, every 100 m from 500 m to 2 km, and
202 every 250 m from 2 to 10 km, AGL). In this study we make use of the NN zenith and of the NN
203 oblique, where the latter can average out small-scale horizontal inhomogeneities of the
204 atmosphere.

205 The MWR-CU operated from 9 March to 7 May 2015, while MWR-NOAA was unavailable
206 between 5-27 April 2015. For the overlapping dates, temperature retrieved from the two
207 MWRs showed very good agreement with less than 0.5 K bias and 0.994 correlation (Bianco et
208 al., 2017). For this reason, we use only the MWR-CU (hereafter simply called MWR).

209

210 **2.2 Radiosonde measurements**

211 Between 9 March and 7 May 2015, while the MWR was operational, radiosondes were
212 launched by the National Center for Atmospheric Research (NCAR) assisted by several students
213 from the University of Colorado over three selected periods, one each in March, April, and May.
214 There was a total of 59 launches, mostly four times per day, around 14:00, 18:00, 22:00 and
215 0200 UTC (8:00, 12:00, 16:00 and 20:00 local standard time, LST). All radiosondes were Vaisala
216 RS92. The first 35 launches, between 9-19 March, were done from the visitor center, while the
217 11 launches, between 15-22 April, and 13 launches, between 1-4 May, were done from the
218 water tank site, ~1000 meters apart (see Lundquist et al., 2017 for a detailed map of the study
219 area). The radiosonde measurements included temperature, dewpoint temperature, and



220 relative humidity, to altitudes usually higher than 10 km AGL, with measurements every few
221 seconds.

222

223 **2.3 WPR-RASS measurements**

224 Two NOAA wind profiling radars (WPRs), operating at frequencies of 915-MHz and 449-
225 MHz, were deployed at the visitor center (same location of the MWR) during XPIA. These
226 systems are primarily designed to measure the vertical profile of the horizontal wind vector, but
227 co-located RASS also observe profiles of virtual temperature in the lower atmosphere, with
228 different resolutions and height coverages depending on the WPR. Thus, the RASS associated
229 with the 915-MHz WPR (hereafter referred to as RASS 915) measured virtual temperature from
230 120 to 1618 m with a vertical resolution of 62 m, and the 449 MHz RASS (hereafter referred to
231 as RASS 449) sampled the boundary layer from 217 to 2001 m with a vertical resolution of 105
232 m. The maximum height reached by the RASS is a function of both radar frequency and
233 atmospheric conditions (May and Wilczak, 1993), and is usually lower for RASS 915 data, as will
234 be shown later in the analysis.

235 The RASS data were processed using a radio frequency interference (RFI)-removal
236 algorithm (performed on the RASS spectra), a consensus algorithm (Strauch et al. 1984)
237 performed on the moment data using a 60% consensus threshold, a Weber-Wuertz outlier
238 removal algorithm (Weber et al., 1993) performed on the consensus averages, and a RASS
239 range-correction algorithm (Görsdorf and Lehmann, 2000) using an average relative humidity
240 setting of 50% determined from the available observations.

241



242 **2.4 BAO data**

243 The BAO 300-m tower was built in 1977 to study the planetary boundary layer (Kaimal
244 and Gaynor 1983). During XPIA, measurements were collected at the surface (2 m) and at six
245 higher levels (50, 100, 150, 200, 250 and 300 m AGL). Each tower level was equipped with 2
246 sonic anemometers on orthogonal booms, and one sensor based on a Sensiron SHT75 solid-
247 state sensor to measure temperature and relative humidity with a time resolution of 1 s, and
248 averaged over five minutes.

249 The observational temperature and water vapor surface data are used from the more
250 accurate observations at the BAO tower 2 m AGL level (Horst, 2016), to replace the data
251 measured by the less accurate MWR inline surface sensor.

252

253

254 **3. Physical retrievals**

255 Other than NN approaches, a physical retrieval (PR) iterative approach can be used to
256 retrieve vertical profiles of thermodynamic properties from the MWR observations (Maahn et
257 al 2020). In this case, using a radiative transfer model, the process starts with a climatologically
258 reasonable value of temperature and water vapor, and is iteratively repeated until the
259 computed brightness temperatures match those observed by the MWR within the uncertainty
260 of the observed brightness temperatures (Rodgers, 2000; Turner and Löhnert, 2014; Maahn et
261 al. 2020).

262



263 **3.1 Iterative retrieval technique**

264 For this study, the physical retrieval (PR) uses a microwave radiative transfer model,
 265 MonoRTM (Clough et al., 2005), which is fully functional for the microwave region and was
 266 intensively evaluated previously on MWR measurements (Payne et al. 2008; 2011). We start
 267 with the state vector $\mathbf{X}_a = [\mathbf{T}, \mathbf{Q}, \text{LWP}]^T$, where superscript T denotes transpose. \mathbf{T} (K) and \mathbf{Q}
 268 (g/kg) are temperature and water vapor mixing ratio profiles at 55 vertical levels from the
 269 surface up to 17 km, with the distance between the levels increasing exponentially-like with
 270 height. LWP is the liquid water path in (g/m²) that measures the integrated content of water in
 271 the entire vertical column above the MWR, and is a scalar. For this study we have \mathbf{X}_a with
 272 dimensions equal to 111 x 1 (two vectors \mathbf{T} and \mathbf{Q} with 55 levels each, and LWP). We are using
 273 the retrieval framework of Turner and Blumberg (2019), but only using MWR data (no spectral
 274 infrared) and will augment the retrieval to include RASS profiles of Tv.

275 The observation vector \mathbf{Y} from the beginning includes temperature and water vapor
 276 mixing ratio measured at the surface, and brightness temperature (\mathbf{T}_b) measured by the MWR.
 277 The MonoRTM model \mathbf{F} is used as the forward model to estimate the observation vector \mathbf{Y} from
 278 the current state vector \mathbf{X} , from Eq. (1), iterating until the difference between $\mathbf{F}(\mathbf{X})$ and \mathbf{Y} is
 279 small within a specified uncertainty:

280
$$\mathbf{X}_{n+1} = \mathbf{X}_a + (\mathbf{S}_a^{-1} + \mathbf{K}^T \mathbf{S}_\varepsilon^{-1} \mathbf{K})^{-1} \mathbf{K}^T \mathbf{S}_\varepsilon^{-1} [\mathbf{Y} - \mathbf{F}(\mathbf{X}_n) + \mathbf{K} (\mathbf{X}_n - \mathbf{X}_a)] \quad (1)$$

281 with:

282
$$\mathbf{X}_a = \begin{bmatrix} \mathbf{T} \\ \mathbf{Q} \\ L \end{bmatrix} \quad \mathbf{S}_a = \begin{bmatrix} \sigma_{TT}^2 & \sigma_{TQ}^2 & 0 \\ \sigma_{QT}^2 & \sigma_{QQ}^2 & 0 \\ 0 & 0 & \sigma_L^2 \end{bmatrix} \quad \mathbf{K}_{ij} = \frac{\partial F_i}{\partial X_j}$$



$$\mathbf{S}_\varepsilon = \begin{bmatrix} \sigma_{T_{sfc}}^2 & 0 & 0 & 0 & 0 & 0 \\ 0 & \sigma_{Q_{sfc}}^2 & \textcircled{1} & 0 & 0 & 0 \\ 0 & 0 & \sigma_{Tb_{zenith}}^2 & 0 & \textcircled{2} & 0 \\ 0 & 0 & 0 & \sigma_{Tb_{zenith+oblique}}^2 & 0 & 0 \\ 0 & 0 & 0 & 0 & 0 & \sigma_{Tv_{RASS915(449)}}^2 \textcircled{3 \text{ or } 4} \end{bmatrix}$$

283

284

and \mathbf{Y} , depending on the configuration used, being equal to:

$$\mathbf{Y}_1 = \begin{bmatrix} T_{sfc} \\ Q_{sfc} \\ \mathbf{T}b_{zenith} \end{bmatrix} \quad \mathbf{Y}_2 = \begin{bmatrix} T_{sfc} \\ Q_{sfc} \\ \mathbf{T}b_{zenith} \\ \mathbf{T}b_{zenith+oblique} \end{bmatrix}$$

285

$$\mathbf{Y}_3 = \begin{bmatrix} T_{sfc} \\ Q_{sfc} \\ \mathbf{T}b_{zenith} \\ \mathbf{T}b_{zenith+oblique} \\ \mathbf{T}v_{RASS915} \end{bmatrix} \quad \mathbf{Y}_4 = \begin{bmatrix} T_{sfc} \\ Q_{sfc} \\ \mathbf{T}b_{zenith} \\ \mathbf{T}b_{zenith+oblique} \\ \mathbf{T}v_{RASS449} \end{bmatrix}$$

286

287

The superscripts T and -1 indicate transpose or inverse matrix, respectively. Also,

288

vectors and matrices are shown in bold. Note that we are including the 2-m surface-level

289

observations of temperature and water vapor mixing ratio (T_{sfc} and Q_{sfc} , respectively) as part

290

of the observation vector \mathbf{Y} , and thus the uncertainties in these observations are included in \mathbf{S}_ε .

291

The first guess of the state vector \mathbf{X} , \mathbf{X}_1 in Eq. (1), is set to be equal to the mean state

292

vector of climatological estimates, or a “prior” vector \mathbf{X}_a , which is calculated independently for

293

each month of the year from climatological sounding profiles (10 years) in the Denver area.

294

\mathbf{S}_a is the covariance matrix of the “prior” vector that includes not only temperature or water

295

vapor variances but also the covariances between them. \mathbf{K} is the Jacobian matrix, computed

296

using finite differences by perturbing the elements of \mathbf{X} and rerunning the radiative transfer

297

model.



298 We start with four configurations for the observational vector \mathbf{Y} (\mathbf{Y}_1 , \mathbf{Y}_2 , \mathbf{Y}_3 , and \mathbf{Y}_4). The
 299 MWR provides the \mathbf{Tb} measurements in all schemes, zenith only in \mathbf{Y}_1 (which also includes the
 300 2-m in-situ observations of temperature and humidity), and zenith and oblique in \mathbf{Y}_2 , \mathbf{Y}_3 , and \mathbf{Y}_4 .
 301 Using additional measurements from the co-located radar systems with RASS, we may further
 302 expand the observational vector with either RASS 915 (\mathbf{Y}_3) or RASS 449 (\mathbf{Y}_4) virtual temperature
 303 observations. The covariance matrix of the observed data, \mathbf{S}_ϵ , depends on the chosen \mathbf{Y}_i as it is
 304 highlighted by the red numbers in the matrix description, with increasing dimensions from \mathbf{Y}_1 to
 305 \mathbf{Y}_2 and additional increasing dimensions to \mathbf{Y}_3 and \mathbf{Y}_4 through the multi-level measurements of
 306 the RASS (Turner and Blumberg, 2019). Table 1 summarizes the observational information
 307 included in these four different configurations of the PR.

	T_{sfc}	Q_{sfc}	T_{bzenith}	$T_{\text{bzenith-oblique}}$	T_{VRASS915}	T_{VRASS449}
$\mathbf{Y}_1 = \text{MWRz}$	X	X	X			
$\mathbf{Y}_2 = \text{MWRzo}$	X	X	X	X		
$\mathbf{Y}_3 = \text{MWRzo915}$	X	X	X	X	X	
$\mathbf{Y}_4 = \text{MWRzo449}$	X	X	X	X		X

308 *Table 1. Four PR configurations corresponding to the four observational \mathbf{Y}_i vectors in Eq. (1).*

309

310 We assume that there is no covariance between different instruments as well as
 311 between different channels (MWR) or height levels (RASS) of each instrument, therefore this
 312 covariance matrix \mathbf{S}_ϵ is diagonal. The Jacobian matrix, \mathbf{K} , has dimensions $m \times 111$, where m is
 313 the length of the vector \mathbf{Y}_i , therefore its dimensions increase correspondingly with the inclusion
 314 of more observational data. \mathbf{K} makes the “connection” between the state vector and the



315 observational data and should be calculated at every iteration.

316

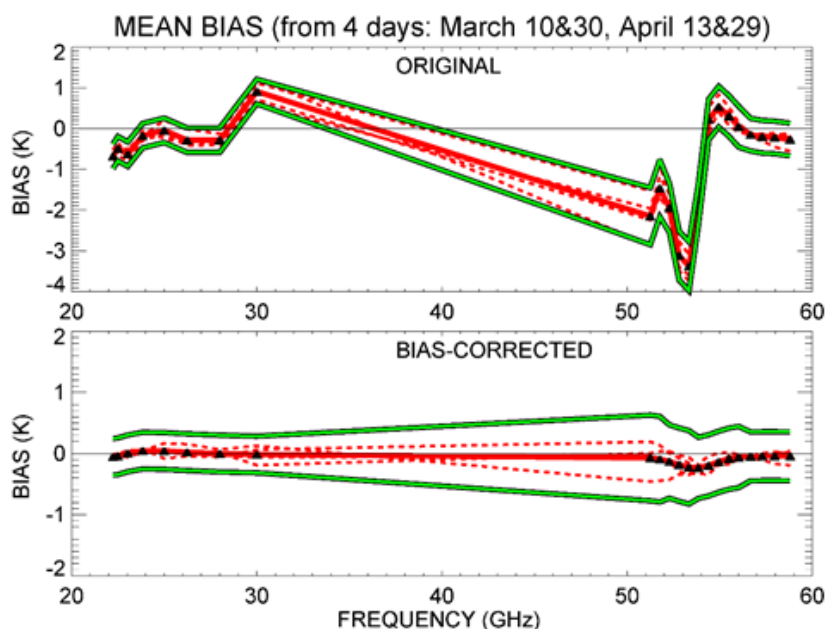
317 **3.2 Bias-correction**

318 Observational errors propagate through the retrieval into the derived profiles (i.e. the
319 bias of the observed data will contribute to bias the retrievals.) For that, retrieval uncertainties
320 in Eq. (1) from $\mathbf{Y} = \mathbf{Y}_1$ or \mathbf{Y}_2 derive only from uncertainties in surface and MWR data, while
321 retrieval uncertainties from $\mathbf{Y} = \mathbf{Y}_3$ or \mathbf{Y}_4 are coming from uncertainties in surface, MWR, and
322 RASS measurements.

323 While the bias of the retrieval depends on both the sensitivity of the forward model and
324 the observational uncertainty, we can try to eliminate, or at least to reduce, the systematic
325 error in the MWR observations. To this aim, we first looked for clear sky days (to reduce the
326 degrees of freedom associated with clouds) during the period of the measurements. One
327 method to identify clear-sky times is to use brightness temperature observations in the 30 GHz
328 water vapor sensitive channel. The random uncertainty in brightness temperature was
329 calculated as its standard deviation during clear sky times and for this channel is approximately
330 0.3 K (but during periods with liquid-bearing clouds overhead, the standard deviation of the 30
331 GHz T_b is markedly higher than this threshold due to the non-homogeneous nature of clouds
332 and thus their contribution to the downwelling microwave radiance). Four clear-sky days were
333 selected, March 10 and 30, and April 13 and 29. The bias was then computed on all channels
334 over these selected clear-sky days and removed from all measurements. Fig. 1 shows the
335 results of the bias-correction for the four chosen clear-sky days. The green lines on this figure
336 indicate the MWR random errors at each frequency calculated as the standard deviation of T_b



337 averaged over one-hour sliding window; these are 0.3-0.4 K for K-band channels and 0.6-0.7 K
338 for V-band channels.



339

340 *Fig.1. Bias for the four chosen clear-sky days (red-dashed lines) and their mean (red solid line)*
341 *for the original observations in the top panel, and for the bias-corrected data in the bottom*
342 *panel. Green lines are the uncertainty boundaries around the mean bias. Frequencies used in the*
343 *PR algorithm are marked with black triangles in both panels.*

344

345 This bias correction was applied to the brightness temperature used in the PR approach;
346 however, the NN retrievals used the uncorrected brightness temperature, since it was non-
347 trivial for us to reprocess those retrievals.



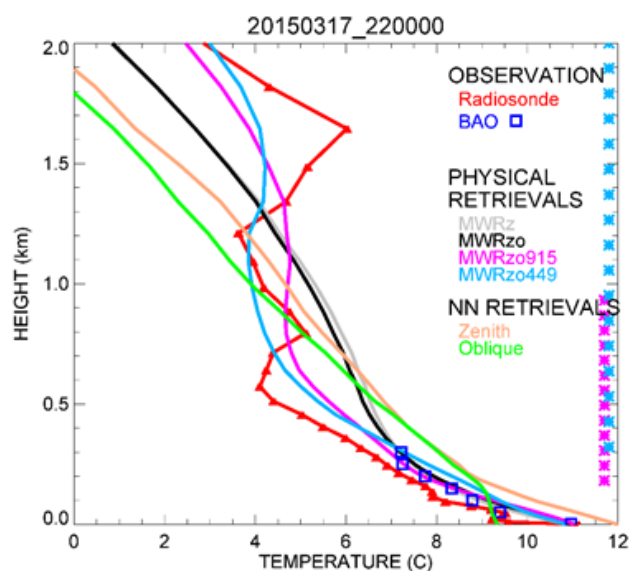
348 The retrieved profiles of the four different PR configurations presented in Table 1
349 (MWRz, MWRzo, MWRzo915, MWRzo449) were compared to the radiosonde profiles, as well
350 as to the NN retrievals. BAO tower temperature and mixing ratio data at the seven available
351 levels were used as an additional validation dataset, without any interpolation.

352 To compare radiosonde observations against the PR and NN retrieved profiles, all these
353 profiles were interpolated vertically to the same PR heights, and PR and NN profiles were
354 averaged in the time window between 15 minutes before and 15 minutes after each
355 radiosonde launch. Since the radiosonde ascends quite quickly in the lowest kilometers of the
356 atmosphere (~15-20 min to reach 5 km), we estimated that the 30-minute temporal window is
357 representative of the same volume of the atmosphere measured by the radiosonde.

358 An example of the different temperature retrievals and their relative performance, data
359 obtained on 17 March 2015 at 2200 UTC is presented in Fig. 2. Temperature profiles up to 2 km
360 AGL from the four PR configurations (MWRz, MWRzo, MWRzo915, MWRzo449) are compared
361 to the radiosonde data in red, to the BAO measurements in blue squares, and to the NN profiles
362 (NN zenith in beige, and NN oblique in green). The MWRz and MWRzo profiles, as well as those
363 from the NNs, are very smooth and depart quite substantially from the radiosonde
364 measurements, being unable to reproduce the more detailed structure of the atmospheric
365 temperature profile measured by the radiosonde, while the MWRzo449 profile (in light-blue)
366 demonstrates better agreement with both the radiosonde and BAO measurements (blue
367 squares). Note that all four of the PRs match the BAO observations reasonably well, while the
368 NN retrievals are warm-biased. The MWRzo915 profile (in magenta) also tries to follow the



369 elevated temperature inversion observed by the radiosonde, successfully only in the lower part
370 of the atmosphere (below 1 km AGL) where RASS 915 measurements are available. This
371 behavior will be also addressed in the following section and in the statistical analysis presented
372 later in the manuscript.



373
374 *Fig. 2. Temperature profiles obtained by the four PR configurations: MWRz in gray, MWRzo in*
375 *black, MWRzo915 in magenta, and MWRzo449 in light-blue; NN retrievals: NN zenith in beige,*
376 *and NN averaged oblique in green. These retrievals are compared to radiosonde measurements,*
377 *in red, and BAO tower observations, in blue squares. The heights with available RASS virtual*
378 *temperature measurements (RASS 915 in magenta and RASS 449 in light-blue), are marked by*
379 *the asterisks on the right Y-axis.*

380

381 3.3 Averaging kernel



382 The averaging kernel, **Akernel** (Masiello et al., 2012, Turner and Löhnert, 2014) from Eq.
383 (1) can be calculated as:

$$384 \quad \mathbf{Akernel} = \mathbf{B}^{-1} \mathbf{K}^T \mathbf{S}_\epsilon^{-1} \mathbf{K} \quad (2)$$

385 where:

$$386 \quad \mathbf{B} = \mathbf{S}_a^{-1} + \mathbf{K}^T \mathbf{S}_\epsilon^{-1} \mathbf{K}$$

387 Both matrices, **Akernel** and **B**, have dimensions 111 x 111 in our configuration. The
388 **Akernel** matrix has useful information about the calculated retrievals, such as vertical
389 resolution and degrees of freedom for signal at each level. Thus, the rows of **Akernel** provide
390 the smoothing functions that have to be applied to the retrievals (Rodgers, 2000) to help
391 minimize the vertical representativeness error in the comparison between the various retrievals
392 and the radiosonde profiles due to very different vertical resolutions of these profiles.

393 Using the averaging kernel, the smoothed radiosonde observed profiles will be
394 therefore computed as:

$$395 \quad \mathbf{X}_{smoothed_sonde} = \mathbf{Akernel} (\mathbf{X}_{sonde} - \mathbf{X}_a) + \mathbf{X}_a \quad (3)$$

396 The **Akernel** in Eq. (2) depends on the retrieval parameters (e.g., which datasets are
397 used in the **Y** vector, the values assumed in the observation covariance matrix \mathbf{S}_ϵ , and the
398 sensitivity of the forward model (i.e., its Jacobian), etc.), so for our four PR configurations it is



399 possible to calculate four different kernels: **A_MWRz**, **A_MWRzo**, **A_MWRzo915** and
400 **A_MWRzo449**, respectively.

401 While the top left corner of the **Akernel** matrix (1:55, 1:55) is devoted to temperature,
402 and it will be called **AT_MWR** hereafter, the next (56:110, 56:110) elements are devoted to
403 water vapor mixing ratio, and will be called **AQ_MWR**.

404 For each of the four **Akernels**, a smoothed radiosonde profile can be computed for each
405 radiosonde profile using Eq. (3). In the presence of temperature inversions or other particular
406 structures in the atmosphere these smoothed profiles can be quite different from each other
407 and also from the original unsmoothed radiosonde profile.

408 Therefore, in the statistical analysis presented later in the manuscript (in section 4.2),
409 mean bias, root mean square error (RMSE), and Pearson correlation coefficients will be
410 computed between the MWR's retrievals and both the unsmoothed and smoothed radiosonde
411 profiles, where the latter were computed using their respective **Akernels**. Additional
412 observational data help to resolve the atmospheric structure in more detail, therefore we
413 would expect to obtain better statistical evaluations from the configurations including
414 additional RASS observations compared to the runs without RASS data.

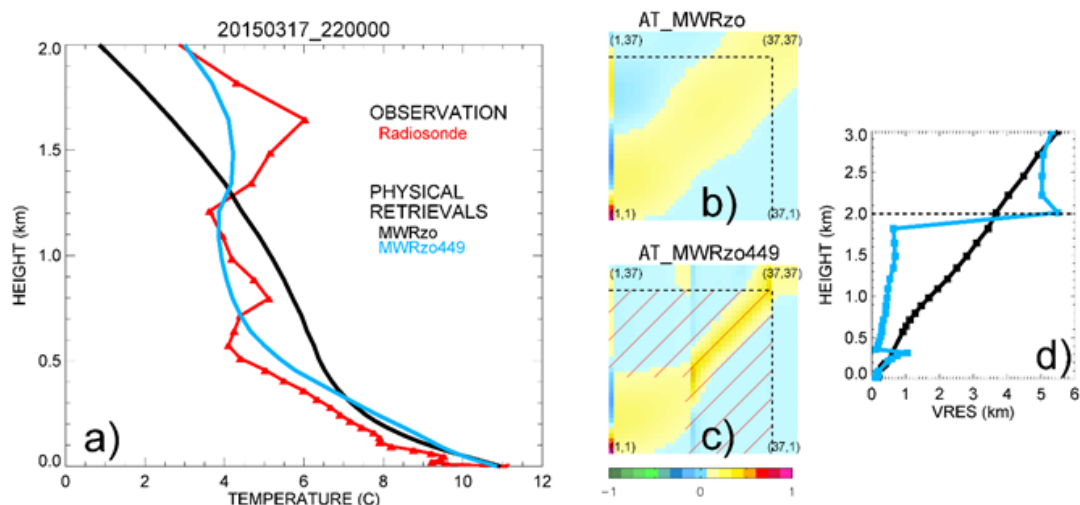
415 The improvement in the retrieved temperature profiles presented in Fig. 2 obtained
416 using additional RASS data can be explained and clearly shown by the **ATkernel** itself. Figure 3
417 includes the temperature profiles of the radiosonde and PRs of MWRzo and MWRzo449 (panel
418 a), and the **ATkernels** corresponding to these PRs in the color plots in the middle of the figure



419 (panels b and c). These color plots are a schematic visualization of the 37 x 37 top left corner of
420 the **ATkernel** matrix that illustrates the part of the **ATkernel** up to 3 km, for reference. Dash
421 lines mark the 2 km vertical level.

422 The rows of the **ATkernel** provide a measure of the retrieval smoothing as a function of
423 altitude, so the full-width half maximum of each **ATkernel** row estimates the vertical resolution
424 of the retrieved solution at each vertical level (Merrelli and Turner, 2012). These plots of
425 temperature vertical resolution vs height for MWRzo and MWRzo449 are included in Figure 3,
426 panel d, for the same case presented in Fig. 2. Comparison of **ATkernel** color plots and vertical
427 resolution plots of MWRzo vs MWRzo449 shows that additional observations from the RASS
428 449 significantly reduces the spread around the main diagonal up to 2 km (in the layer of the
429 atmosphere where RASS 449 measurements are available), thereby improving the vertical
430 resolution of the retrievals (as clearly visible in panel d).

431



432



433 *Fig. 3. Panel a: temperature profiles from radiosonde, in red, from MWRzo PR in black, and from*
434 *MWRzo449 PR in light-blue. Middle colored panels: 37x37 levels (surface to 3 km) of the Akernel*
435 *matrix for temperature, b) AT_MWRzo and c) AT_MWRzo449. Right panel d: vertical resolution*
436 *(VRES) as a function of the height for the MWRzo PR (black), and for the MWRzo449 PR (light-*
437 *blue). Dash lines on plots b)-d) mark 2 km AGL. Hatched area on panel c) marks the RASS*
438 *measurement heights.*

439

440 **4. Results**

441 PR and NN retrieved profiles have been evaluated against radiosonde observations. For
442 additional verification, radiosonde data from 59 launches taken between 9 March and 4 May
443 2015 were first of all compared to the BAO tower measurements, up to 300 m AGL. These
444 observed data sets match very well, with a correlation coefficient of 0.99 and a standard
445 deviation of ~ 0.7 °K. However, one radiosonde profile showed a large bias (> 5 °K) against all
446 seven levels of BAO temperature measurements and against all PRs and NNs, therefore we
447 decided to exclude this particular radiosonde profile from the statistical calculations.

448

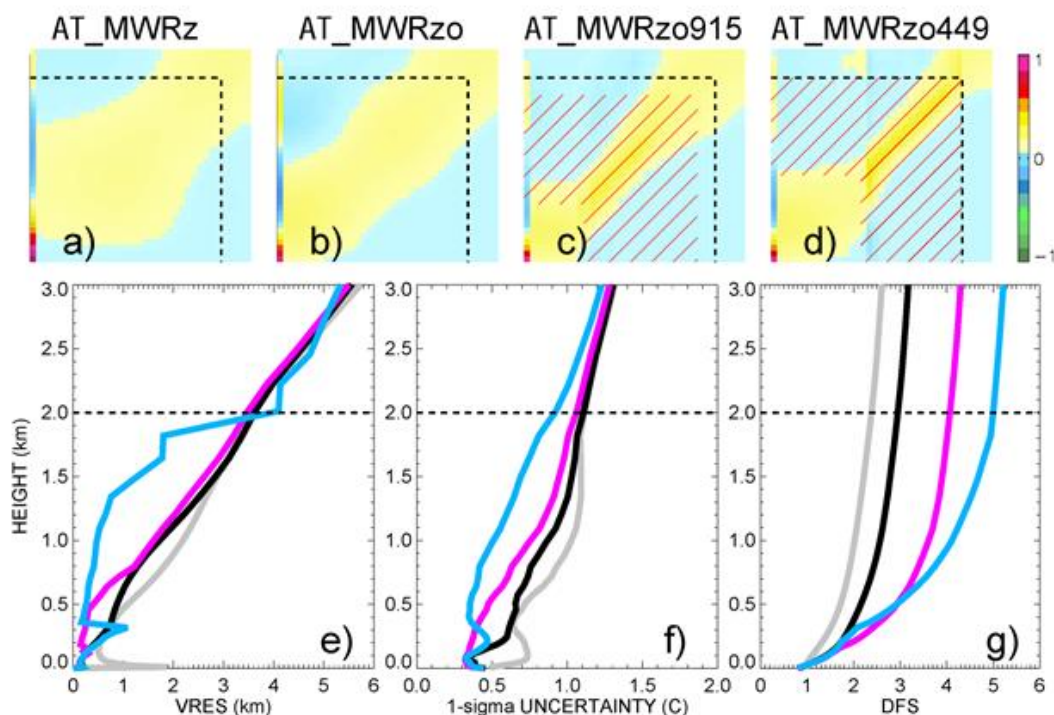
449 **4.1 PRs statistical analysis**

450 To complete the analyses on the **ATkernel** changes and dependencies from different
451 types of observational data used in the PRs, the **ATkernels**, averaged over all radiosonde
452 events, are shown in Fig. 4, panels a-d, for the four PR configurations of Table 1, in the same
453 way as shown in Fig. 3, b-c. A clearly visible gradual narrowing of the spread around the main
454 diagonal is obtained by the usage of the additional observations, from MWR zenith only (panel



455 a), to MWR zenith-oblique (panel b), to the larger impact obtained by the usage of RASS 915
456 (panel c) and RASS 449 (panel d) data.

457 Other statistically important features to analyze in the PRs, besides vertical resolution,
458 are the retrieval uncertainty, and the degree of freedom for signal (DFS). These three features
459 are also shown in Fig.4, panels e-g, at each of the heights of the retrieved solution, up to 3 km
460 AGL, and averaged over all radiosonde events. While the vertical resolution (panel e) shows the
461 width of the atmosphere layer used for each retrieval height (the vertical resolution is
462 computed as the full-width half-maximum value of the averaging kernel), the uncertainty (panel
463 f) gives a measure of the retrieval correctness (computed by propagating the uncertainty of the
464 observations and the sensitivity of the forward model), and the DFS (panel g) is a measure of
465 the number of independent pieces of information used in the retrieved solution. For example,
466 at the 1 km AGL level the vertical resolution of MWRzo449 equals 0.5 km, i.e. information from
467 +/- 0.5 km around the retrieval height are considered in the retrieval, while all other retrievals
468 use the information from +/- 2 km. Also, the uncertainty of the MWRzo449 retrieval up to 1km
469 AGL is around 0.5 °K while the other retrievals have higher uncertainties of up to 1 °K. The
470 higher accuracy of the MWRzo449 retrievals is because they use more observational
471 information compared to the other retrieval configurations.



472

473 Fig. 4. Top four-color images: **AT** kernels for MWRz (panel a), MWRzo (panel b), MWRzo915
474 (panel c) and MWRzo449 (panel d), averaged over all radiosonde events. Hatched area on
475 panels c) and d) marks the RASS measurement heights. Bottom three panels from left to right:
476 vertical resolution (VRES) in km (panel e), one-sigma uncertainty derived from the posterior
477 covariance matrix in °C (panel f), and cumulative Degree of Freedom (DFS, panel g) as a function
478 of height for temperature, averaged over all radiosonde events (MWRz is in gray, MWRzo is in
479 black, MWRzo915 is in magenta, and MWRzo449 is in light-blue). Dash lines mark 2 km AGL on
480 all panels.

481

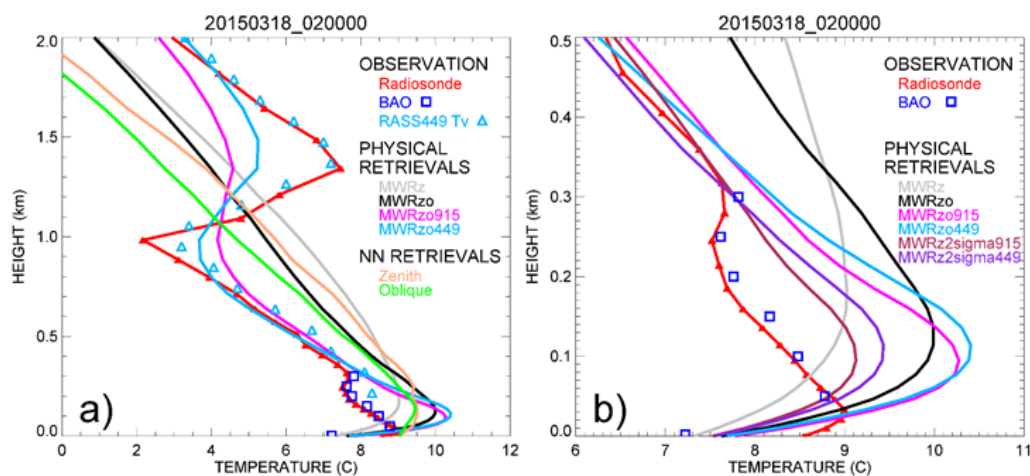


482 The improvements from MWRz (in gray) to MWRzo (in black), then to MWRzo915 (in
483 magenta), and finally to MWRzo449 (in light-blue) are visible in all three panels (Fig 4 e-g),
484 whereas MWRzo449 has the best statistical measures compared to the other PRs, particularly
485 below 2 km AGL, where RASS 449 measurements are available. Finally, it is interesting that
486 below 200 m AGL the MWRzo915 has slightly better statistics compared to the MWRzo449, as
487 could be expected due to the first available height of the RASS 915 being lower (120 m AGL)
488 than the first available height for the RASS 449 (217 m AGL) and due to the finer vertical
489 resolution of the 915-MHz RASS. This suggests that if additional observations were available in
490 the lowest several 100 m layer of the atmosphere where RASS measurements are not available,
491 improvements might be even better closer to the surface, where temperature inversions, if
492 present, are sometimes difficult to retrieve correctly.

493 As a matter of fact, we found several cases during XPIA when the temperature profile
494 exhibits inversions, with the lowest happening in the surface layer. Figure 5a shows one of the
495 most complex cases, with several temperature inversions visible in the temperature profile
496 from the radiosonde (red line), in the temperature measurements from the BAO tower (blue
497 squares), and in the virtual temperature measured by the RASS 449 (light blue triangles). We
498 note that the virtual temperature profile is in close agreement with the temperature measured
499 by radiosonde. Generally, the moisture contribution to the virtual temperature is less than a
500 degree K, decreasing substantially for dryer air. Among the PR profiles, the PRs including RASS
501 data show better agreement with the radiosonde in the atmospheric layer where RASS
502 measurements are available, as was already shown in Fig. 2 for a different date. Unfortunately,
503 this better performance is not visible below the first available RASS measurement, i.e. from the



504 surface up to ~200m AGL, where the PRs with additional RASS data have the largest positive
505 bias compared to both radiosonde and BAO data in this layer. We believe that the MWR data,
506 especially those from the oblique scans, in this case have a bias in the observed brightness
507 temperatures that propagates through the retrieval calculations, and including other
508 observational data is not enough to correct it in the layer between the surface data and the first
509 available RASS measurement.



510

511 *Fig. 5. Panel a) as in Fig. 2 but for 18 March 2015 at 0200 UTC. The RASS 449 virtual*
512 *temperature is included as light blue triangles. Panel b) shows the same data (except for the NN*
513 *retrievals) presented in panel a), but only up to 500 m AGL, and includes PR profiles in which the*
514 *MWR uncertainties were increased by a factor of two, MWRz915 in maroon and MWRz449 in*
515 *violet.*

516



517 After several trials, we found that when RASS measurements are included, temperature
518 profiles in this and similar cases exhibiting inversions could be improved by increasing the
519 random uncertainty of MWR observations, and only using the zenith MWR measurements,
520 because the oblique MWR brightness temperature measurements (which give more
521 information in the lower layer of the atmosphere) seemingly have a bias that competes with
522 the active and more accurate measurements from the RASS and surface observations. In this
523 way, the PR approach is granted more freedom to get an optimal profile in the gap between the
524 lowest RASS measurements and the surface measurement. Proof of this is presented in Figure
525 5b, that shows the same data as in 5a, but including the profiles obtained when increasing the
526 assumed MWR Tb uncertainties by a factor of two, hereafter called MWRz2sigma915 and
527 MWRz2sigma449, in maroon and violet respectively. The increased accuracy of these
528 temperature profiles compared to MWRzo915 and MWRzo449 are obvious in the layer of
529 atmosphere closer to the surface. Later we will show that these last two PR configurations
530 demonstrate improved statistics over all 58 cases, and also through the layer of the atmosphere
531 up to 5km. We note that these last two PR configurations, that were found to work well for this
532 dataset, might not be optimal for other datasets. During XPIA the RASS measurements impact
533 (particularly those from the RASS 449) was important in the PR approach. This might not be the
534 case for other datasets or over different seasons, when RASS coverage might not be as good as
535 that during XPIA. For this reason, we think that attention has to be used to determine what is
536 the best configuration to use when dealing with PR approaches. On the positive side, the
537 advantage is that the user can determine and has control on what is the optimal configuration
538 to use in his/her dataset, in terms of different inputs to employ and their relative uncertainty.

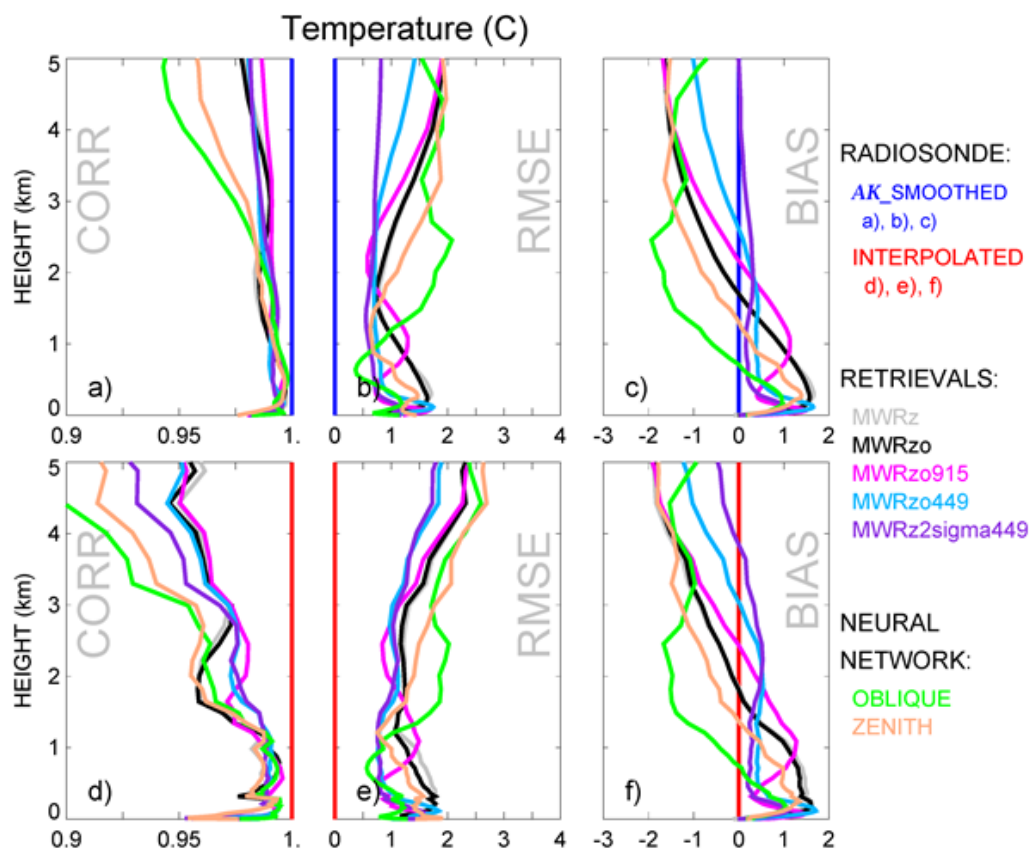


539

540 **4.2 Statistical analysis of PRs compared to NN retrievals**

541 Since the iteratively calculated PRs and the NN retrievals are obtained by very different
542 approaches, we find it very important to compare their relative statistical behavior. We do this
543 both for temperature and mixing ratio, providing this comparison in two ways: first using the
544 **Akernel** smoothed radiosonde data obtained as described in section 3.3, and second comparing
545 to the original, unsmoothed, radiosonde profiles, just interpolated to the 55 PR vertical levels.

546 Figure 6 shows the statistical results of these comparisons for temperature, in terms of
547 Pearson correlation, RMSE, and mean bias, averaged over all radiosonde events.



548

549 Fig. 6. Pearson correlation, RMSE, and mean bias for temperature profiles of MWRz in gray,
550 MWRzo in black, MWRzo915 in magenta, MWRzo449 in light-blue and MWRz2sigma449 in
551 violet, computed comparing to smoothed radiosonde data (using their relative **ATkernel**) in
552 panels a-c, and against the original radiosonde measurements in panels d-f. The same
553 comparisons for NN profiles, with NN zenith in beige, and NN averaged oblique in green, are
554 made against the corresponded smoothed radiosonde data in the top panel and against original
555 radiosonde data in the bottom panel.



556

557 These results confirm the superiority of the MWRz2sigma449 temperature retrieval
558 over the other PRs. While this is not true at all heights, this retrieval shows improved
559 distribution of RMSE and bias for the atmospheric layer up to 5 km AGL. The MWRz2sigma915
560 profile is not included in the figure to not overcrowd it, but its behaviour compared to the
561 MWRzo915 is similar to that of the MWRz2sigma449 compared to the MWRzo449 profile,
562 reducing the drastic bias found in the layer closer to the ground. The differences between the
563 two ways of comparison, against the smoothed **ATkernel** or the original radiosonde data, are
564 small in terms of RMSE and bias, but more evident in terms of correlation as it can be expected
565 because of the smoothing technique applied to the radiosonde profiles through Eq. (3). Above
566 and below 1.5 km AGL the bias, RMSE, and correlation profiles of the PRs show very different
567 behavior. While statistical measures above 1.5 km AGL are very similar for the four PRs
568 introduced in Table 1, they are better for the MWRz2sigma449 PR, especially when compared
569 to the smoothed radiosonde profiles. Differences between the profiles show more variability in
570 the lowest 1.5 km. NN retrievals, both for zenith and averaged oblique, are very variable from
571 height to height and generally have much larger RMSE and bias, and worse correlation
572 coefficients compared to PRs.

573 Besides temperature profiles, the NN and PR retrievals also provide water vapor mixing
574 ratio profiles. It is understandable that the different configurations of PRs are not noticeably
575 different from each other in relation to moisture, because the Tv observations from the RASS
576 are dominated by the ambient temperature (not moisture), and thus have little impact on the
577 water vapor retrievals.

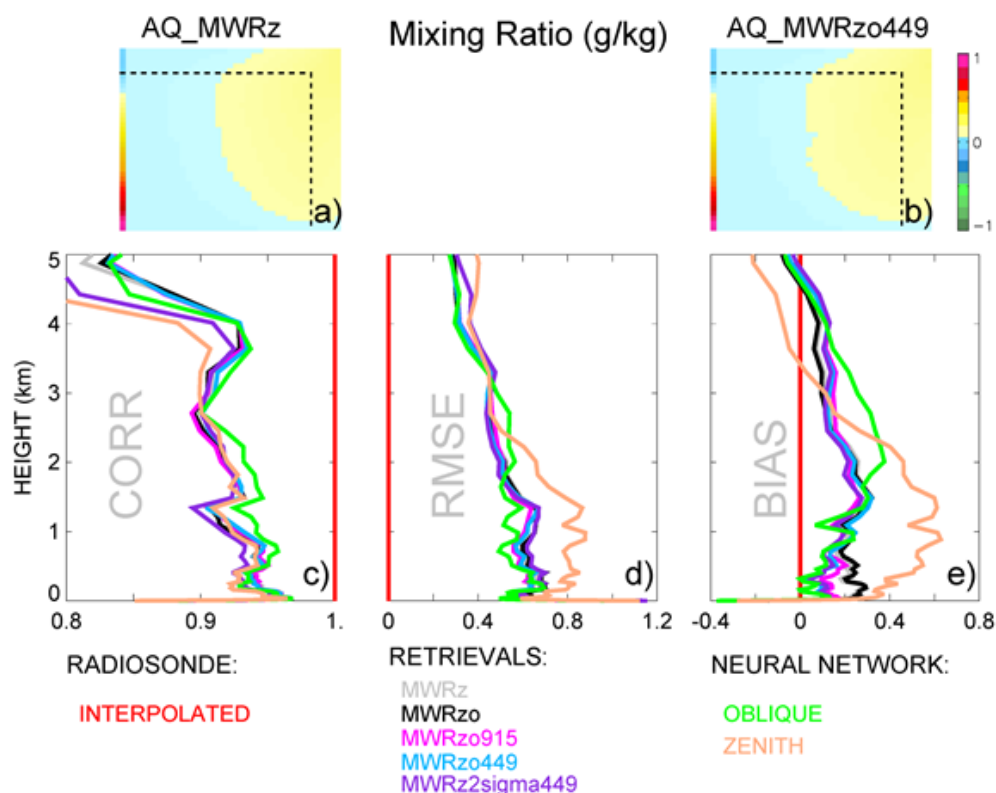


578 Figure 7 includes two **AQkernels** corresponding to the PRs MWRz and MWRzo449 in
579 panels a and b, which are averaged over all radiosonde events and appear to be almost
580 identical. More detailed statistical estimations of PRs mixing ratio in Fig 7 c-e, also averaged
581 through all radiosonde events, show very similar correlations, RMSEs, and biases for all PRs
582 included in the figure, meaning that the impact of including RASS observations is minimal on
583 this variable. These PR mixing ratio profiles are also statistically very close to the averaged
584 oblique NN retrieval mixing ratio profiles, with the zenith NN retrieval mixing ratio profiles
585 showing the worst statistics in terms of RMSE and bias. Overall, we conclude that the PR
586 retrievals are not degraded on average compared to the NN moisture retrievals.

587

588

589



590

591 *Fig. 7. Top two-color images: AQ kernels for MWRz (panel a) and MWRzo449 (panel b),*
 592 *averaged over all radiosonde events and shown up to 3 km AGL with dash lines mark 2 km AGL*
 593 *on both panels. Bottom three panels are the same as panels d-f in Figure 6, but for mixing ratio*
 594 *estimation.*

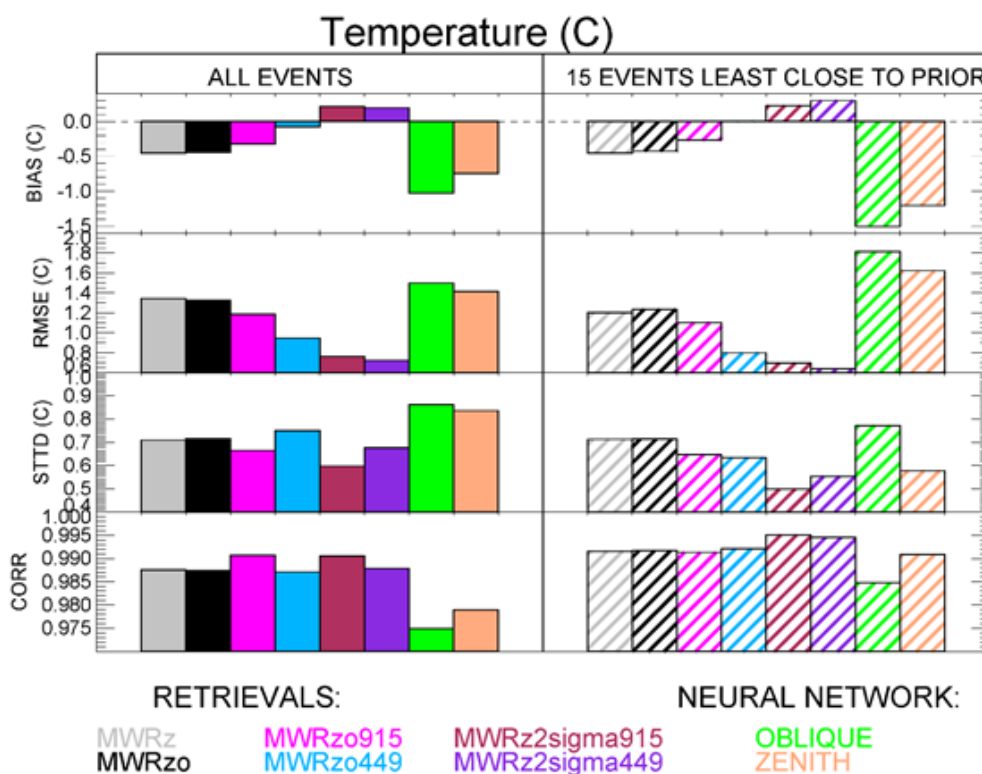
595

596 4.3 Statistics for cases far from the climatological mean

597 While both approaches, physical and neural network retrievals, are quite different, both
 598 use climatological data as a constraint or for building the statistical relationships used in the
 599 retrieval. Statistically, the averaged profiles of both temperature and moisture variables are



600 very close to the climatological averages. However, the most interesting and difficult profiles to
 601 retrieve are the cases furthest from the climatology (Löhnert and Maier, 2012). To check the
 602 behavior of the retrieved data in such events, we first calculated the RMSE for each radiosonde
 603 profile relative to the prior profiles for 42 vertical levels from the surface up to 5 km AGL, and
 604 then we selected the 15 cases with the largest 0-5km layer averaged RMSEs compared to the
 605 prior. All comparisons are done against the corresponded smoothed **ATkernel** radiosonde data,
 606 using **AT_MWRz**, **AT_MWRzo**, **AT_MWRzo915**, **AT_MWRzo449**, **AT_MWRz2sigma915**,
 607 **AT_MWRz2sigma449** for all six PRs, and **AT_MWRz**, **AT_MWRzo** for NN zenith and NN oblique
 608 retrievals respectively.
 609



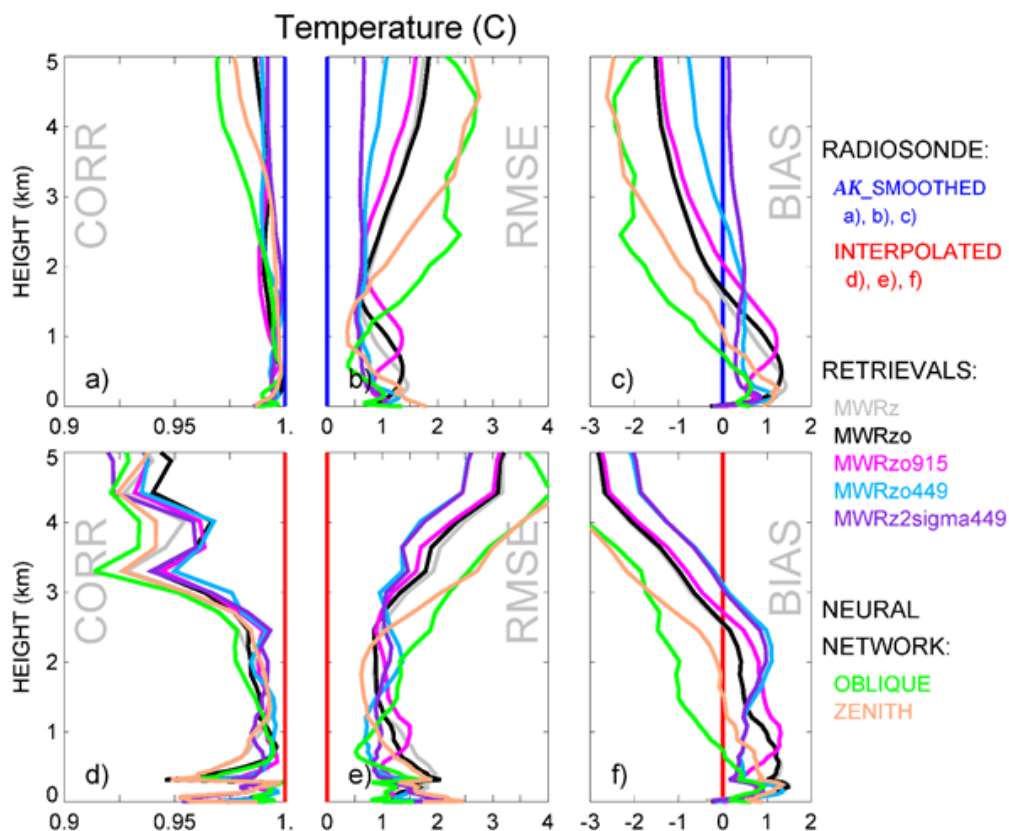
610



611 *Fig. 8. From top to bottom: biases (retrievals minus ATkernel radiosonde), RMSEs, standard*
612 *deviations of the difference between retrievals and ATkernel radiosonde, and Pearson*
613 *correlations for the six PR configurations so far introduced and both NN retrievals, averaged*
614 *from the surface to 5 km AGL, averaged over all radiosonde data (solid boxes), and averaged*
615 *over the 15 events furthest from the priors (hatched boxes).*

616

617 Figure 8 shows the temperature statistical analysis for the entire radiosonde data set
618 (solid boxes) and to just the fifteen chosen events (hatched boxes) for bias, RMSE, standard
619 deviation of retrieval differences to the radiosonde data, and Pearson correlation, calculated as
620 the weighted averaged over the 42 vertical heights up to 5 km AGL. Differences in the statistics
621 when using the entire radiosonde data set or the fifteen profiles furthest from the prior are
622 noticeable, especially for bias and RMSE, but also for the standard deviation. All PRs that
623 include RASS observations show better performance compared to strictly MWR-only PR profiles
624 (i.e., MWRz and MWRzo) for almost all statistical comparisons. Also, the statistical behavior of
625 the MWRz2sigma915 and MWRz2sigma449 retrievals are the best in terms of RMSE and
626 standard deviation for all events and for RMSE, standard deviation, and correlation coefficient,
627 for the fifteen profiles furthest from the climatological average. Finally, we note that the NN
628 profiles are the least accurate retrievals for all of the statistics for the entire radiosonde data
629 set, and have the highest bias, RMSE and the lowest correlation for the 15 events.



630

631 *Fig. 9. The same as Fig. 6 but for the temperature over 15 furthest from prior radiosonde*
632 *profiles.*

633

634 To investigate the vertical structure of the error statistics for the 15 events furthest from
635 the radiosonde climatology, profiles of correlation, RMSE and bias for these events are shown
636 in Figure 9 for the layer 0-5 km. The MWRz449 and MWRz2sigma449 profiles, which were seen
637 in Fig. 8 to have the best layer averaged statistics, are seen to be as good as, or better, than the
638 other methods for the 0-2 km layer. Importantly, for heights above 2km AGL, where there is no



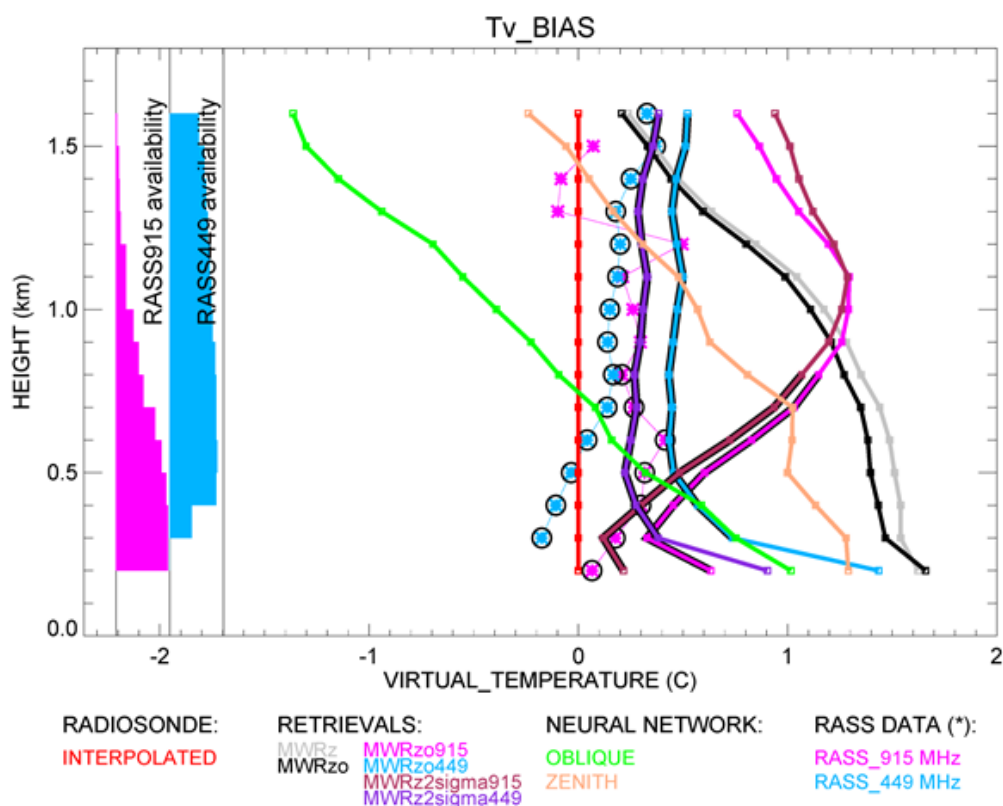
639 additional observational data from RASS, all of the PRs are better than the NN profiles, with the
640 MWRz2sigma449 and MWRz449 being the best. We note that the increased accuracy of the
641 PRs relative to the NNs is more obvious in Fig. 9 for the 15 events when compared to the entire
642 data set in Fig. 6. Also, it can be seen that the NNs for the 15 events are worse than they are
643 for the entire data set, especially in the 2-5km layer, which indicates (not surprisingly) that the
644 NNs accuracy degrades when the atmosphere is far from its climatology.

645

646 **4.4 Virtual temperature statistics**

647 The above analysis confirms the superiority of MWRz2sigma915 and MWRz2sigma449
648 compared to the other PRs and to the NN retrievals for this dataset. In this section we show the
649 direct comparison of the retrieved profiles to the original radiosonde and RASS virtual
650 temperature profiles. Using temperature and moisture retrieval output, we calculated
651 “retrieved virtual temperature profiles” and interpolated all profiles and RASS data on a regular
652 vertical grid, going from 200 m to 1.6 km with 100 m range, for easy comparison.

653 Figure 10 shows T_v retrieved profile biases compared to the original radiosonde data as
654 solid lines, and RASS 915 and RASS 449 T_v bias as asterisks. A zero bias is denoted by the red
655 line. On the left side of the figure we show bar charts of the RASS measurement availability as a
656 function of height. The widest part of these charts corresponds to 100% data availability.
657 Heights with RASS availability greater than 50% are marked with additional circles over the
658 asterisks.



659

660 *Fig. 10. Bias of virtual temperature for all six PR configurations and both NN retrievals*

661 *compared to the original radiosonde measurements. RASS data are marked by asterisks and by*

662 *additional circles for the RASS data with more than 50% availability, according to the availability*

663 *bar charts on the left.*

664

665 While RASS 449 data are available at almost all heights up to 1.6 km, the RASS 915 data

666 availability decreases considerably with height, lowering to 50% availability around 800 m AGL.

667 All PRs with input from RASS data, MWRzo915 and MWRzo449, and MWRz2sigma915 and

668 MWRz2sigma449 with larger MWR uncertainties, are also marked with additional black lines at



669 the heights with at least 50% of relative RASS data availability. This figure clearly shows the
670 superiority of MWRz2sigma449 and MWRz2sigma915 (in the layer with > 50% RASS 915 data
671 availability) compared to MWRz and MWRzo configurations, which do not include RASS data, as
672 well as to MWRzo915 and MWRzo449 which include RASS data and MWR zenith and oblique
673 data. For MWRzo449 and MWRz2sigma449 profiles, RASS 449 data were almost always
674 available, therefore it is easy to identify similar features between Tv bias profiles of the RASS
675 449 and the PRs including it. Thus, for the MWRzo449 and MWRz2sigma449 the Tv bias is more
676 uniform through the heights compared to all other PRs that do not include RASS data, and to
677 both NN retrievals. Moreover, because MWRzo449 and MWRz2sigma449 Tv bias profiles follow
678 tightly the trend of the RASS 449 with height, the difference between MWRzo449 and RASS 449
679 biases equals ~ 0.32 °C and the difference between MWRz2sigma449 and RASS 449 biases
680 equals ~ 0.14 °C over the ~ 1.3 km atmospheric layer where RASS 449 measurements are
681 available, uniformly distributed through the heights. Finally, the average differences between
682 these MWRzo449 and MWRz2sigma449 Tv profiles and the radiosonde virtual temperature
683 equal ~ 0.56 °C and ~ 0.34 °C respectively. From these results we can assume that the final bias
684 of the PRs that include additional RASS data derives from a combination of the RASS data bias
685 itself, of the uncertainty of the retrieval model, and of the MWR brightness temperature biases,
686 even though we tried to correct for the latter.

687 We note as an alternative to using the PR temperatures at all heights, one could
688 consider replacing the PR temperatures with RASS observations up to the maximum height
689 reached by the RASS, and then use the PR retrieval above that. To do this the moisture



690 contribution to the RASS virtual temperatures could be removed by using either the relative
691 humidity measured by radiometer or by a climatology of the moisture term.

692

693 5. Conclusions

694 In this study we used the data collected during the XPIA field campaign to test different
695 configurations of a physical-iterative retrieval (PR) approach in the determination of
696 temperature and humidity profiles from data collected by microwave radiometers, surface
697 sensors, and RASS measurements. We tested the accuracy of several PR configurations, two
698 that made use only of surface observations and MWR observed brightness temperature (zenith
699 only, MWRz, and zenith plus oblique, MWRzo), and others that included the active observations
700 available from two co-located RASS (one, RASS 915, associated with a 915-MHz, and the other,
701 RASS 449, associated with a 449-MHz wind profiling radar). Radiosonde launches were used for
702 verification of the retrieved profiles and Neural Network retrieved profiles were also used for
703 comparison. The NN retrievals used in this study were obtained either using the zenith angle
704 only, or the average of the oblique scans (based on the averaged T_b of 15- and 165-degree
705 scans) without including the zenith. Other MWR systems (Rose et al., 2005) provide retrieved
706 profiles that include the information from both oblique and zenith scans.



707 Inclusion of the observations from the active RASS instruments in the PR approach
708 improves the accuracy of the temperature profiles, particularly when low-level temperature
709 inversions are present. Of the PRs configurations tested, we find better statistical agreement
710 with the radiosonde observations when the RASS 449 is used together with the surface
711 observations and brightness temperature from only the zenith MWR observations
712 (MWRz2sigma449), and doubling the random radiometric uncertainty on the MWR
713 observations relative to the uncertainty calculated over the selected clear-sky days (Fig. 1). This
714 configuration is also more accurate compared to MWRzo915 or MWRz2sigma915 (which use
715 RASS 915 observation), because of the deeper RASS 449 height coverage. The larger assumed
716 radiometric uncertainty in the MWR Tb observations allows the retrieval to overcome both (a)
717 the (small) systematic errors that exist between the MWR (which could be in either the
718 observed Tb values or in the MonoRTM used as the forward model) and the RASS, and (b) the
719 systematic errors that exist in forward microwave radiative models (Cimini et al. 2018).

720 We also selected 15 cases when temperature profiles from the radiosonde observations
721 were the furthest from the mean climatological average, and reproduced the statistical
722 comparison over this subset of cases. These are the cases usually most difficult to retrieve and
723 most important to forecast; therefore, it is essential to improve the retrievals in these
724 situations. Even for this subset of selected cases we find that MWRz2sigma449 produces better
725 statistics, proving that the inclusion of active sensor observations in MWR passive observations



726 would be beneficial for improving the accuracy of the retrieved temperature profiles also in the
727 upper layer of the atmosphere where RASS measurements are not available (at least up to 5 km
728 AGL).

729 Finally, we also considered the impact of the inclusion of RASS measurements on the
730 retrieved humidity profiles, but in this case the inclusion of RASS observations did not produce
731 significantly better results, compared to the configurations that do not include them. This was
732 not a surprise as RASS measures virtual temperature, effectively adding very little extra
733 information to the water vapor retrievals. In this case a better option would be to consider
734 adding other active remote sensors such as water vapor differential absorption lidars (DIALs) to
735 the PRs. Turner and Löhnert (2020) showed that including the partial profile of water vapor
736 observed by the DIAL substantially increases the information content in the combined water
737 vapor retrievals. Consequently, to improve both temperature and humidity retrievals a synergy
738 between MWR, RASS, and DIAL systems would likely be necessary.

739

740 **Data availability**

741 All data are publicly accessible at the DOE Atmosphere to Electrons Data Archive and
742 Portal, found at <https://a2e.energy.gov/projects/xpia> (Lundquist et al., 2016).

743

744 **Author contribution**



745 Irina Djalalova completed the primary analysis with physical retrieval approach through
746 MONORTM using XPIA data. Daniel Gottas contributed to the post-processing of the RASS data.
747 Irina Djalalova prepared the manuscript with contributions from all co-authors.

748

749 **Acknowledgements**

750 We thank all the people involved in XPIA for instrument deployment and maintenance,
751 data collection, and data quality control, and particularly the University of Colorado Boulder for
752 making the CU MWR data available. Funding for this study was provided by the NOAA/ESRL
753 Atmospheric Science for Renewable Energy (ASRE) program.

754

755

756

757 **References**

758 Adachi, A. and H. Hashiguchi, 2019: Application of parametric speakers to radio acoustic
759 sounding system. *Atmos. Meas. Tech.*, **12**, 5699–5715, 2019,
760 <https://doi.org/10.5194/amt-12-5699-2019>.
761 Adler, B., J. M. Wilczak, L. Bianco, I. Djalalova, J. B. Duncan Jr., D. D. Turner, 2020: Observational
762 case study of a persistent cold air pool and gap flow in the Columbia River Basin. *In*
763 *preparation*.



- 764 Banta, R. M., and coauthors, 2020: Characterizing NWP model errors using Doppler lidar
765 measurements of recurrent regional diurnal flows: Marine-air intrusions into the
766 Columbia River Basin. *Month. Wea. Rev.*, **148**, 927-953, doi:10.1175/MWR-D-19-0188.1
- 767 Blumberg, W. G., D. D. Turner, S. M. Cavallo, J. Gao, J. Basara, A. Shapiro, 2019: An Analysis of
768 the Processes Affecting Rapid Near-Surface Water Vapor Increases during the Afternoon
769 to Evening Transition in Oklahoma. *J. of Appl. Meteorol. and Climatol.*, **58(10)**, 2217–
770 2234, <https://doi.org/10.1175/JAMC-D-19-0062.1>.
- 771 Bianco L., D. Cimini, F. S. Marzano, and R. Ware, 2005: Combining microwave radiometer and
772 wind profiler radar measurements for high-resolution atmospheric humidity profiling, *J.*
773 *Atmos. Ocean. Tech.*, **22**, 949–965, <https://doi.org/10.1175/JTECH1771.1>.
- 774 Bianco, L., K. Friedrich, J. M. Wilczak, D. Hazen, D. Wolfe, R. Delgado, S. Oncley, and J. K.
775 Lundquist, 2017: Assessing the accuracy of microwave radiometers and radio acoustic
776 sounding systems for wind energy applications. *Atmos. Meas. Tech.*, **10**, 1707-1721,
777 <https://doi.org/10.5194/amt-10-1707-2017>.
- 778 Cadeddu, M. P., J. C. Liljegren, and D. D. Turner, 2013: The Atmospheric radiation measurement
779 (ARM) program network of microwave radiometers: instrumentation, data, and
780 retrievals, *Atmos. Meas. Tech.*, **6**, 2359–2372, [https://doi.org/10.5194/amt-6-2359-](https://doi.org/10.5194/amt-6-2359-2013)
781 [2013](https://doi.org/10.5194/amt-6-2359-2013).
- 782 Cimini, D., M. Haeffelin, S. Kotthaus, U. Löhnert, P. Martinet, E. O'Connor, C. Walden, M.
783 Collaud Coen, and J. Preissler, 2020: Towards the profiling of the atmospheric boundary
784 layer at European scale—introducing the COST Action PROBE. *Bulletin of Atmospheric*
785 *Science and Technology*, **1**, 23–42, <https://doi.org/10.1007/s42865-020-00003-8>.



- 786 Cimini, D., Rosenkranz, P. W., Tretyakov, M. Y., Koshelev, M. A., and Romano, F., 2018:
787 Uncertainty of atmospheric microwave absorption model: impact on ground-based
788 radiometer simulations and retrievals, *Atmos. Chem. Phys.*, **18**, 15231–15259,
789 <https://acp.copernicus.org/articles/18/15231/2018/>.
- 790 Clough, S.A., M. W. Shephard, E. J. Mlawer, J. S. Delamere, M. Iacono, K. E. Cady-Pereira, S.
791 Boukabara and P. D. Brown: Atmospheric radiative transfer modeling: A summary of the
792 AER codes, *JQSRT*, vol 91, no. 2, pp 233-244, 2005,
793 <https://doi.org/10.1016/j.jqsrt.2004.05.058>.
- 794 Engelbart, D., W. Monna, J. Nash, 2009: Integrated Ground-Based Remote-Sensing Stations for
795 Atmospheric Profiling, *COST Action 720 Final Report*, EUR 24172,
796 <https://doi.org/10.2831/10752>.
- 797 Görzdorf, U., and V. Lehmann, 2000: Enhanced Accuracy of RASS-Measured Temperatures Due
798 to an Improved Range Correction. *J. Atmos. Oceanic Technol.*, **17** (4), 406–416,
799 [https://doi.org/10.1175/1520-0426\(2000\)017<0406:EAORMT>2.0.CO;2](https://doi.org/10.1175/1520-0426(2000)017<0406:EAORMT>2.0.CO;2).
- 800 Han, Y., and E. R. Westwater, 1995: Remote sensing of tropospheric water vapor and cloud
801 liquid water by integrated ground-based sensors. *J. Atmos. Oceanic Tech.*, **12**, 1050-
802 1059.
- 803 Han, Y., and E. R. Westwater, 2000: Analysis and improvement of tipping calibration for ground-
804 based microwave radiometers. *IEEE Trans. Geosci. Remote Sens.*, **38**, 1260–1276,
805 <https://doi.org/10.1109/36.843018>.
- 806 Horst, T. W., S. R. Semmer, and I. Bogoev, 2016: Evaluation of Mechanically-Aspirated
807 Temperature/Relative Humidity Radiation Shields, *18th Symposium on Meteorological*



- 808 *Observation and Instrumentation, AMS Annual Meeting, New Orleans, LA, 10-15 January*
809 2016, <https://ams.confex.com/ams/96Annual/webprogram/Paper286839.html>.
- 810 Kaimal, J. C., and J. E. Gaynor, 1983: The Boulder Atmospheric Observatory. *J. Climate Appl.*
811 *Meteor.*, **22**, 863–880, [https://doi.org/10.1175/1520-](https://doi.org/10.1175/1520-0450(1983)022<0863:TBAO>2.0.CO;2)
812 [0450\(1983\)022<0863:TBAO>2.0.CO;2](https://doi.org/10.1175/1520-0450(1983)022<0863:TBAO>2.0.CO;2).
- 813 Kuchler, N., D. D. Turner, U. Löhnert, and S. Crewell, 2016: Calibrating ground-based microwave
814 radiometers: Uncertainty and drifts, *Radio Sci.*, **51**, 311–
815 327, [doi:10.1002/2015RS005826](https://doi.org/10.1002/2015RS005826).
- 816 Löhnert U. and O. Maier, 2012: Operational profiling of temperature using ground-based
817 microwave radiometry at Payerne: prospects and challenges. *Atmos. Meas. Tech.*, **5**,
818 1121–1134, <https://doi.org/10.5194/amt-5-1121-2012>.
- 819 Lundquist, J. K., J. M. Wilczak, R. Ashton, L. Bianco, W. A. Brewer, A. Choukulkar, A. Clifton, M.
820 Debnath, R. Delgado, K. Friedrich, S. Gunter, A. Hamidi, G. V. Iungo, A. Kaushik, B.
821 Kosović, P. Langan, A. Lass, E. Lavin, J. C.-Y. Lee, K. L. McCaffrey, R. K. Newsom, D. C.
822 Noone, S. P. Oncley, P. T. Quelet, S. P. Sandberg, J. L. Schroeder, W. J. Shaw, L. Sparling,
823 C. St. Martin, A. St. Pe, E. Strobach, K. Tay, B. J. Vanderwende, A. Weickmann, D. Wolfe,
824 and R. Worsnop, 2017: Assessing state-of-the-art capabilities for probing the
825 atmospheric boundary layer: the XPIA field campaign. *Bull. Am. Meteor. Soc.*, **98**, 289–
826 314, <https://doi.org/10.1175/BAMS-D-15-00151.1>.
- 827 Maahn, M., D. D. Turner, U. Löhnert, D. J. Posselt, K. Ebell, G. G. Mace, and J. M. Comstock,
828 2020: Optimal estimation retrievals and their uncertainties: What every atmospheric



- 829 scientist should know. *Bull. Amer. Meteor. Soc.*, **101**, E1512-E1523, doi:10.1175/BAMS-
830 D-19-0027.1
- 831 May P. T., Moran, K. P., and Strauch, R. G., 1989: The Accuracy of RASS Temperature
832 Measurements, *J. Appl. Meteorol.*, **28**, 1329–1335.
- 833 May, P. T. and J. M. Wilczak, 1993: Diurnal and Seasonal Variations of Boundary-Layer Structure
834 Observed with a Radar Wind Profiler and RASS. *Mon. Wea. Rev.*, **121**, 673–682,
835 [https://doi.org/10.1175/1520-0493\(1993\)121<0673:DASVOB>2.0.CO;2](https://doi.org/10.1175/1520-0493(1993)121<0673:DASVOB>2.0.CO;2).
- 836 Masiello, G., C. Serio, and P. Antonelli, 2012: Inversion for atmospheric thermodynamical
837 parameters of IASI data in the principal components space. *Quart. J. Roy. Meteor. Soc.*,
838 **138**, 103–117, <https://doi.org/10.1002/qj.909>.
- 839 Merrelli, A. M., and D. D. Turner, 2012: Comparing information content of upwelling far infrared
840 and midinfrared radiance spectra for clear atmosphere profiling. *J. Atmos. Oceanic
841 Technol.*, **29**, 510–526, <https://doi.org/10.1175/JTECH-D-11-00113.1>.
- 842 Neiman, P. J., D. J. Gottas, and A. B. White, 2019: A Two-Cool-Season Wind Profiler–Based
843 Analysis of Westward-Directed Gap Flow through the Columbia River Gorge. *Month.
844 Wea. Rev.*, **147**, 4653-4680, <https://doi.org/10.1175/MWR-D-19-0026.1>.
- 845 North, E. M., A. M. Peterson, and H. D. Parry, 1973: RASS, a remote sensing system for
846 measuring low-level temperature profiles. *Bull. Am. Meteor. Soc.*, **54**, 912–919.
- 847 Payne, V. H., J. S. Delamere, K. E. Cady-Pereira, R. R. Gamache, J.-L. Moncet, E. J. Mlawer, and S.
848 A. Clough, 2008: Air-broadened half-widths of the 22- and 183-GHz water-vapor lines.
849 *IEEE Trans. Geosci. Remote Sens.*, **46**, 3601-3617, doi:10.1109/TGRS.2008.2002435.



- 850 Payne, V. H., E. J. Mlawer, K. E. Cady-Pereira, and J.-L. Moncet, 2011: Water vapor continuum
851 absorption in the microwave. *IEEE Trans. Geosci. Remote Sens.*, **49**, 2194-2208,
852 doi:10.1109/TGRS.2010.2091416. Rodgers, C. D., 2000: Inverse Methods for Atmospheric
853 Sounding: Theory and Practice. *Series on Atmospheric, Oceanic and Planetary Physics*,
854 Vol. 2, World Scientific, 238 pp.
- 855 Rose, T., S. Crewell, U. Löhnert, C. Simmer, 2005: A network suitable microwave radiometer for
856 operational monitoring of the cloudy atmosphere, *Atmospheric Research*, **75**, Issue 3,
857 183–200, <https://doi.org/10.1016/j.atmosres.2004.12.005>.
- 858 Rosenkranz, P. W., 1998: Water vapour microwave continuum absorption: A comparison of
859 measurements and models. *Radio Science*, **33**, 919–928.
- 860 Shaw, W., and Coauthors, 2019: The Second Wind Forecast Improvement Project (WFIP 2):
861 General Overview. *Bull. Am. Meteor. Soc.*, **100(9)**, 1687–1699,
862 <https://doi.org/10.1175/BAMS-D-18-0036.1>.
- 863 Solheim, F., J. R. Godwin, J., and R. Ware, 1998a: Passive ground-based remote sensing of
864 atmospheric temperature, water vapor, and cloud liquid profiles by a frequency
865 synthesized microwave radiometer. *Meteorol. Z.*, **7**, 370–376.
- 866 Solheim F., J. R. Godwin, E. R. Westwater, Y. Han, S. J. Keihm, K. Marsh, R. Ware, 1998b:
867 Radiometric profiling of temperature, water vapor and cloud liquid water using various
868 inversion methods. *Radio Science*, **33**, 393–404, <https://doi.org/10.1029/97RS03656>.



- 869 Stankov, B. B., E. R. Westwater, and E. E. Gossard, 1996: Use of wind profiler estimates of
870 significant moisture gradients to improve humidity profile retrieval. *J. Atmos. Oceanic*
871 *Tech.*, **13**, 1285-1290.
- 872 Strauch, R. G. , D. A. Merritt, K. P. Moran, K. B. Earnshaw, and D. V. De Kamp, 1983: The
873 Colorado wind-profiling network. *J. Atmos. Oceanic Technol.*, **1**, 37–49,
874 [https://doi.org/10.1175/1520-0426\(1984\)001<0037:tcwpm>2.0.co;2](https://doi.org/10.1175/1520-0426(1984)001<0037:tcwpm>2.0.co;2).
- 875 Turner, D. D., and U. Löhnert, 2014: Information content and uncertainties in thermodynamic
876 profiles and liquid cloud properties retrieved from the ground-based Atmospheric
877 Emitted Radiance Interferometer (AERI). *J. Appl. Meteor. Clim.*, **53**, 752–771,
878 <https://doi.org/10.1175/JAMC-D-13-0126.1>.
- 879 Turner, D. D., and W. G. Blumberg, 2019: Improvements to the AERIoe thermodynamic profile
880 retrieval algorithm. *IEEE Journal of Selected Topics in Applied Earth Observations and*
881 *Remote Sensing*, **12(5)**, 1339–1354, <https://doi.org/10.1109/JSTARS.2018.2874968>.
- 882 Turner, D. D., and U. Löhnert, 2020: Ground-based Temperature and Humidity Profiling:
883 Combining Active and Passive Remote Sensors. *In revision to Atmos. Meas. Tech.*
884 *Discuss.*, <https://doi.org/10.5194/amt-2020-352>.
- 885 Ware R., Solheim F., Carpenter R., and Coauthors, 2003: A multi-channel radiometric profiler of
886 temperature, humidity and cloud liquid. *Radio Science*, **38**, No. 4, 8079,
887 <https://doi.org/10.1029/2002RS002856>.



- 888 Weber, B. L. , D. B. Wuertz, D. C. Welsh, and R. Mcpeek, 1992: Quality controls for profiler
889 measurements of winds and RASS temperatures. *J. Atmos. Oceanic Technol.*, **10**, 452–
890 464, [https://doi.org/10.1175/1520-0426\(1993\)010<0452:qcfpmo>2.0.co;2](https://doi.org/10.1175/1520-0426(1993)010<0452:qcfpmo>2.0.co;2)
- 891 Wilczak, J. M., and Coauthors, 2019: The Second Wind Forecast Improvement Project (WFIP2):
892 Observational Field Campaign. *Bull. Am. Meteor. Soc.*, **100(9)**, 1701–1723,
893 <https://doi.org/10.1175/BAMS-D-18-0035.1>.
- 894 Wolfe, D. E. and R. J. Latatits, 2018: Boulder Atmospheric Observatory: 1977–2016: The end of
895 an era and lessons learned. *Bull. Am. Meteor. Soc.*, **99**, 1345–1358,
896 <https://doi.org/10.1175/BAMS-D-17-0054.1>.